Mu-Chieh, Lo, Guzmán, Robinson, Carpintero, Guillermo. (2018). Femtosecond pulse and terahertz two-tone generation from facet-free multi-segment laser diode in InP-based generic foundry platform. *Optics Express*, 26(14), pp. 18386-18398.

DOI: https://doi.org/10.1364/OE.26.018386

Femtosecond pulse and terahertz two-tone generation from facet-free multi-segment laser diode in InP-based generic foundry platform

MU-CHIEH LO,* ROBINSON GUZMÁN, AND GUILLERMO CARPINTERO

Departamento de Tecnología Electrónica, Universidad Carlos III de Madrid, Avda. Universidad, 30. 28911 Leganés, Madrid, Spain
mlo@ing.uc3m.es

Abstract: In this paper, a monolithically integrated ~1.55 μm semiconductor laser in the fourth harmonic colliding pulse mode locking configuration is reported. This device was developed within a multi-project wafer run at an InP-based active-passive generic foundry. The 1.66-mm Fabry-Pérot cavity is formed with two on-chip reflector building blocks rather than cleaved facets. In the cavity, three absorber sections symmetrically divide the cavity in four gain segments. This laser diode is able to emit 100-GHz pulse trains with 500-fs pulse duration as well as two-tone emissions with a frequency separation of 2.7 THz. The dependence of the spectral behavior on the forward bias current for gain sections and the reverse bias voltage for absorber sections are experimentally demonstrated.

OCIS codes: (140.4050) Mode-locked lasers; (140.5960) Semiconductor lasers; (250.5300) Photonic integrated circuits.

References and links

1. E. Avrutin, J. Marsh, and E. Portnoi, "Monolithic and multi-gigahertz mode-locked semiconductor lasers: constructions, experiments, models and applications," IEE Proceedings-Optoelectronics **147**, 251–278 (2000).
2. P. J. Delfyett, A. Ardey, S. P. Bhooplapur, and E. Sarailou, "Inp-based device technologies for signal processing using ultrafast frequency combs," IEEE J. Sel. Top. Quantum Electron. **24**, 1–13 (2018).
3. M.-C. Lo, R. C. G. Martínez, and G. Carpintero, "Monolithic mode locked laser-based optical frequency comb for ofdm integrated on inp generic technology platform," in "Optical Fiber Communication Conference," (Optical Society of America, 2018), pp. Th1I–1.
4. J. H. Marsh and L. Hou, "Mode-locked laser diodes and their monolithic integration," IEEE J. Sel. Top. Quantum Electron. **23**, 1–11 (2017).
5. Y. K. Chen, M. C. Wu, T. TanbunâĂŘEk, R. A. Logan, and M. A. Chin, "Subpicosecond monolithic collidingâĂŘpulse modeâĂŘlocked multiple quantum well lasers," Appl. Phys. Lett. **58**, 1253–1255 (1991).
6. E. A. Avrutin, J. H. Marsh, J. M. Arnold, T. F. Krauss, H. Pottinger, and R. M. D. la Rue, "Analysis of harmonic (sub) thz passive mode-locking in monolithic compound cavity fabry-perot and ring laser diodes," IEE Proc. - Optoelectronics **146**, 55–61 (1999).
7. S. Arahira, S. Oshiba, Y. Matsui, T. Kunii, and Y. Ogawa, "Terahertz-rate optical pulse generation from a passively mode-locked semiconductor laser diode," Opt. letters **19**, 834–836 (1994).
8. S. Arahira, S. Oshiba, Y. Matsui, T. Kunii, and Y. Ogawa, "500 ghz optical short pulse generation from a monolithic passively mode-locked distributed bragg reflector laser diode," Appl. physics letters **64**, 1917–1919 (1994).
9. Y. Katagiri and A. Takada, "A harmonic colliding-pulse mode-locked semiconductor laser for stable subterahertz pulse generation," IEEE Photonics Technol. Lett. **9**, 1442–1444 (1997).
10. J. F. Martins-Filho, E. A. Avrutin, C. N. Ironside, and J. S. Roberts, "Monolithic multiple colliding pulse mode-locked quantum-well lasers, experiment and theory," IEEE J. Sel. Top. Quantum Electron. **1**, 539–551 (1995).
11. L. Hou, M. Haji, and J. H. Marsh, "240 ghz pedestal-free colliding-pulse mode-locked laser with a wide operation range," Laser Phys. Lett. **11**, 115804 (2014).
12. E. Kleijn, M. K. Smit, and X. J. Leijtens, "Multimode interference reflectors: a new class of components for photonic integrated circuits," J. Light. Technol. **31**, 3055–3063 (2013).
13. S. Stopinski, M. Malinowski, R. Piramidowicz, C. Kazmierski, M. K. Smit, and X. J. Leijtens, "Photonic integrated multichannel wdm modulators for data read-out units," J. Light. Technol. **32**, 3879–3887 (2014).
14. D. dâĂŹAgostino, D. Lenstra, H. Ambrosius, and M. Smit, "Coupled cavity laser based on anti-resonant imaging via multimode interference," Opt. letters **40**, 653–656 (2015).

15. P. E. Morrissey, N. Kelly, M. Dernaika, L. Caro, H. Yang, and F. H. Peters, "Coupled cavity single-mode laser based on regrowth-free integrated mmi reflectors," IEEE Photonics Technol. Lett **28**, 1313–1316 (2016).
16. N. P. Kelly, M. Dernaika, L. Caro, P. E. Morrissey, A. H. Perrott, J. K. Alexander, and F. H. Peters, "Regrowth-free single mode laser based on dual port multimode interference reflector," IEEE Photonics Technol. Lett. **29**, 279–282 (2017).
17. M.-C. Lo, R. Guzmán, and G. Carpintero, "Inp femtosecond mode-locked laser in a compound feedback cavity with a switchable repetition rate," Opt. Lett. **43**, 507–510 (2018).
18. M.-C. Lo, R. Guzmán, C. Gordón, and G. Carpintero, "Mode-locked laser with pulse interleavers in a monolithic photonic integrated circuit for millimeter wave and terahertz carrier generation," Opt. Lett. **42**, 1532–1535 (2017).
19. C. Gordón, R. Guzmán, V. Corral, X. Leijtens, and G. Carpintero, "On-chip colliding pulse mode-locked laser diode (occp-mlld) using multimode interference reflectors," Opt. Express **23**, 14666–14676 (2015).
20. M.-C. Lo, R. Guzmán, M. Ali, R. Santos, L. Augustin, and G. Carpintero, "1.8-thz-wide optical frequency comb emitted from monolithic passively mode-locked semiconductor quantum-well laser," Opt. letters **42**, 3872–3875 (2017).
21. M. J. Heck, E. A. Bente, Y. Barbarin, A. Fryda, H.-D. Jung, Y.-S. Oei, R. Notzel, D. Lenstra, and M. K. Smit, "Characterization of a monolithic concatenated soa/sa waveguide device for picosecond pulse amplification and shaping," IEEE J. Quantum Electron. **44**, 360–369 (2008).
22. D. Wake, C. R. Lima, and P. A. Davies, "Optical generation of millimeter-wave signals for fiber-radio systems using a dual-mode dfb semiconductor laser," IEEE Transactions on microwave Theory Tech. **43**, 2270–2276 (1995).
23. N. Kim, S.-P. Han, H. Ko, Y. A. Leem, H.-C. Ryu, C. W. Lee, D. Lee, M. Y. Jeon, S. K. Noh, and K. H. Park, "Tunable continuous-wave terahertz generation/detection with compact 1.55 μm detuned dual-mode laser diode and ingaas based photomixer," Opt. express **19**, 15397–15403 (2011).
24. N. Kim, S.-P. Han, H.-C. Ryu, H. Ko, J.-W. Park, D. Lee, M. Y. Jeon, and K. H. Park, "Distributed feedback laser diode integrated with distributed bragg reflector for continuous-wave terahertz generation," Opt. express **20**, 17496–17502 (2012).
25. M. Smit, X. Leijtens, H. Ambrosius, E. Bente, J. van der Tol, B. Smalbrugge, T. de Vries, E.-J. Geluk, J. Bolk, R. van Veldhoven, L. Augustin, P. Thijs, D. DâĂŹAgostino, H. Rabbani, K. Lawniczuk, S. Stopinski, S. Tahvili, A. Corradi, E. Kleijn, D. Dzibrou, M. Felicetti, E. Bitincka, V. Moskalenko, J. Zhao, R. Santos, G. Gilardi, W. Yao, K. Williams, P. Stabile, P. Kuindersma, J. Pello, S. Bhat, Y. Jiao, D. Heiss, G. Roelkens, M. Wale, P. Firth, F. Soares, N. Grote, M. Schell, H. Debregeas, M. Achouche, J.-L. Gentner, A. Bakker, T. Korthorst, D. Gallagher, A. Dabbs, A. Melloni, F. Morichetti, D. Melati, A. Wonfor, R. Penty, R. Broeke, B. Musk, and D. Robbins, "An introduction to inp-based generic integration technology," Semicond. Sci. Technol. **29**, 083001 (2014).
26. L. M. Augustin, R. Santos, E. den Haan, S. Kleijn, P. J. A. Thijs, S. Latkowski, D. Zhao, W. Yao, J. Bolk, H. Ambrosius, S. Mingaleev, A. Richter, A. Bakker, and T. Korthorst, "Inp-based generic foundry platform for photonic integrated circuits," IEEE J. Sel. Top. Quantum Electron. **24**, 1–10 (2018).
27. V. Moskalenko, S. Latkowski, S. Tahvili, T. de Vries, M. Smit, and E. Bente, "Record bandwidth and sub-picosecond pulses from a monolithically integrated mode-locked quantum well ring laser," Opt. Express **22**, 28865–28874 (2014).
28. S. Latkowski, V. Moskalenko, S. Tahvili, L. Augustin, M. Smit, K. Williams, and E. Bente, "Monolithically integrated 2.5 ghz extended cavity mode-locked ring laser with intracavity phase modulators," Opt. letters **40**, 77–80 (2015).
29. P. Stolarz, J. Javaloyes, G. Mezosi, L. Hou, C. Ironside, M. Sorel, A. Bryce, and S. Balle, "Spectral dynamical behavior in passively mode-locked semiconductor lasers," IEEE Photonics J. **3**, 1067–1082 (2011).

1. Introduction

Passive mode locking (PML) using III-V semiconductor lasers in photonic integrated circuits (PIC) generating optical frequency combs (OFC) and ultrafast pulse trains have attracted attention in recent years, due to its chip-scaled compactness and simplicity of DC operation. Especially, PML at repetition rates (RR) in millimeter-wave (mmW, 30-300 GHz) and terahertz (THz, 0.1-10 THz) ranges have been considered promising in communications, spectroscopy, and sensing [1–3]. However, in most cases an extremely high RR (>100 GHz) of a mode-locked lasers (MLL) is corresponding to only a few hundreds of μm cavity length (<400 μm). And such a short gain medium inevitably imposes a limitation on the output power due to saturation effects and insufficient gain to compensate for resonator losses. For this reason, harmonic mode locking (HML) schemes have been investigated to produce multiple pulses per round trip in a sufficiently long cavity, thus pushing the RR beyond the low-GHz fundamental cavity round trip frequency [4].

HML is achieved by means of colliding pulse ML [5], coupled cavity ML [6], and methods based on the wavelength selectivity of distributed Bragg reflector (DBR) grating [7]. The same research group also observed that higher-order harmonic ML occurs at high bias level [8]. In

colliding pulse ML, one saturable absorber is placed at the midpoint of cavity, where two counter propagating pulses circulate and collide, producing a train of pulses at a RR that is twice the fundamental round trip frequency. Evolving from colliding pulse ML, multiple colliding pulse ML features multiple saturable absorbers concatenated with gain sections, for RR multiplication >2 as has been extensively investigated [9–11].

Edge facets have been used as mirrors to realize a multiple colliding pulse ML cavity, as they are relatively easy to make by cleaving the chips, unlike using DBRs as mirrors that requires a costly sub-wavelength fabrication process. However, for design reproducibility, high precision cleaving is seriously needed which hinders the practicability. Besides, laser signals are emitted directly out of the chips through cleaved facets, making on-chip signal processing impossible.

Recently, a new class of on-chip broadband reflector based on the multimode interference (MMI) principle has been proposed [12], and demonstrated its wide applicability [13–17]. Such multimode interference reflector (MIRs) are so simple to create in lithography with greater fabrication tolerance to replace DBRs and cleaved facets. Furthermore, they can be placed anywhere on a chip, and the transmitted light is manipulable on chip to fulfill more functionalities [18].

MIRs have been therefore adopted in on-chip colliding pulse mode locking [19, 20], but none of these works has reached balanced and higher (>2) order operation for pulse amplification and reshpaing [21]. In this paper, we report a monolithically integrated MIR-based fourth harmonic colliding pulse MLL in a symmetric configuration. In addition to generating the fourth harmonic OFC and ultrafast pulse trains, even higher-order harmonic operations are observed at aforementioned higher bias levels [8]. It is worth highlighting again that this terahertz-rate emission based on higher-order harmonic generation does not require any grating-based DFB or DBR component [22–24]. This laser chip was developed within a multi-project wafer (MPW) run in a generic foundry platform [25, 26], where the MIRs, gain sections, and saturable absorbers were deployed as standard building blocks called from the open-access process design kit (PDK) for cost-effective prototyping.

2. Device description

Figure 1(a) shows that the device under investigation is a multi-section structure. The laser cavity is formed with a pair of MIRs, in which there are four gain sections separated by three saturable absorber sections, placed at every quarter of the cavity length. The on-chip reflectors MIRs, define a cavity length (L) of ~1.66 mm, corresponding to a cavity round trip frequency of ~25 GHz. Every quarter (L/4) is ~0.42 mm long.

Gain sections and absorber sections are realized using the same active type building block, semiconductor optical amplifier (SOA). When a SOA is forward-biased it behaves as a gain section. And when reverse-biased, it serves as a saturable absorber (SA), which absorbs light at low intensity and transmits light at high intensity. In the design, all three SAs are as short as 20 μm. The two inner gain sections, which are much longer (~350 μm) than the two outer gain sections ~180 μm. Each of the gain and the SA sections has a metal deposition layer. The metal pads (green) are contiguously connected through metal routes (red) to their symmetric reflections with respect to the central SA, as shown in Fig. 1(b). Electrical isolation sections were inserted between every two adjacent SOAs to avoid unfavorable current flows.

At each end of the cavity, one 2-port MIR terminates the straight waveguide at one port defining the overall Fabry-Pérot cavity length, but also guides the resonating light out of the cavity through the other port. The two MIRs are ~55-μm long, having two ports with ~40% transmissivity and ~40% reflectivity, based on the multimode interference principle and internal etched reflection walls [12]. For retaining the quarter geometry, ~75-μm passive deeply etched waveguides were used between the outer gain sections and the 2-port-MIRs. Also, active-passive transition sections were used to couple light through butt-joint regrowths.

(a)

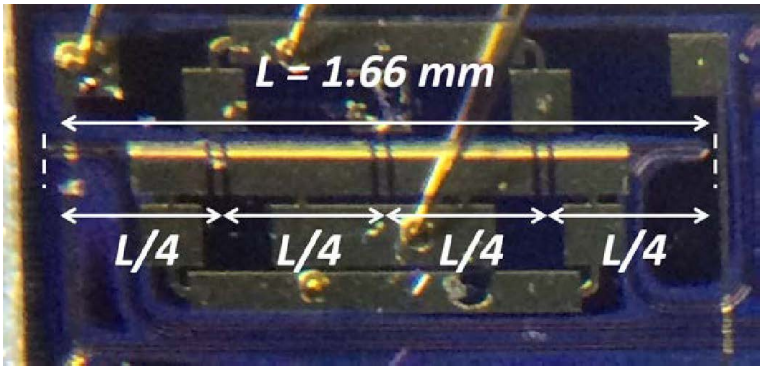

(b)

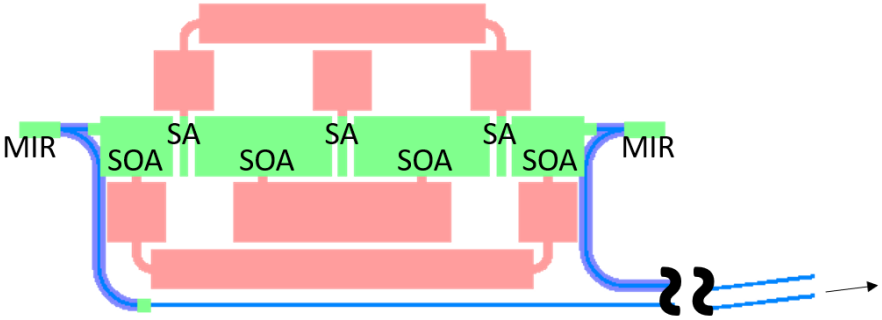

Fig. 1: (a) The total cavity length L ~ 1.66 mm is separated with three saturable absorbers that equally divide the cavity in four, L/4 ~ 0.42 mm. (b) The Fabry-Pérot cavity defined by two multimode interference reflectors (MIR, green) has longer SOAs as gain sections (SOA) and shorter SOAs as saturable absorbers (SA). The extended connection of active components (green) is carried out with DC routing (red). The passive waveguides (blue) also contribute to the cavity length and direct the light to the waveguide outputs at facet.

As there are two MIRs, the light exits from the cavity from both sides. The light from the left MIR travels along a 90◦ arc waveguide prior to a straight-arc-straight connector waveguide , and heads towards a waveguide output at facet. The shallowly etched waveguide output is 7◦ upwards angled and tapered to minimize back-reflections at facet. A lensed fiber couples the emitted light from the microchip to one of the measuring instruments.

To control the integrated device, all SOAs are electrically connected with external current or voltage sources. Four DC probe are physically contacted on the four DC pad extensions for outer gain sections, outer absorber sections, inner gain sections, and inner absorber section, respectively, as shown in Fig. 2(a). Consequently, the voltage of all the three SAs is set through the two upper pads which are jointly connected to an external voltage source (V_{SA}). Similarly, the two lower pads are fed with one common source from a laser diode driver that delivers a current (I_{SOA}) shared by all the four gain sections in parallel. The backside of the substrate is grounded, and TEC-controlled at 16◦ with the same laser diode driver.

Figure 2(b) illustrates that the two input parameters, reverse-bias voltage V_{SA} and forward-bias current I_{SOA} determine the operation state of the MLL PIC under test. The output signal from PIC

(a)

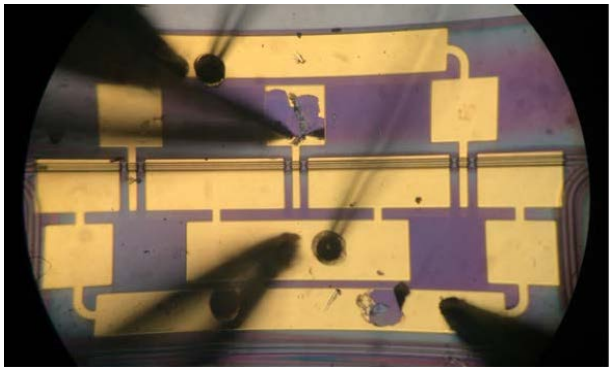

(b)

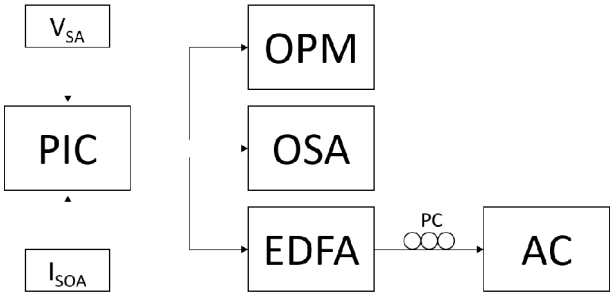

Fig. 2: (a) One DC probe needle electrically contacts each of the four DC pads. (b) The device under test is controlled with the voltage source V_{SA} and the current source I_{SOA}. The output pulse train is evaluated using the optical power meter (OPM), the optical spectrum analyzer (OSA), and the autocorrelator (AC). The polarization controller (PC) and the EDFA must be used to satisfy the polarization state and sensitivity of AC.

is analyzed with the measuring instruments. From the angled waveguide output, the fiber-coupled optical signal is sent to either an optical power meter (OPM), an optical spectrum analyzer (OSA), or an intensity autocorrelator (AC) following an erbium-doped fiber amplifier (EDFA) linked with a polarization controller (PC). The OPM provides the intensity information, essential in evaluating output power level of the MLL as well as the alignment of fiber coupling. The OSA visualizes and records an optical spectrum with a resolution of 0.03 nm. The EDFA boosts the optical power to ~5 dBm to meet the sensitivity requirement of the AC. The PC is used to optimize the polarization dependence.

3. Characterization results

Figure 3(a) presents the L-I-V characteristics. The reverse bias voltage V_{SA} is either switched off (= 0 V) or biased with 1 V, and the forward bias gain current I_{SOA} is varied from 0 to 200 mA in a step of 10 mA to present the dependence of voltage of the gain sections (green) and the fiber-coupled power (red and blue) on the gain current I_{SOA}. The threshold current is around 40 mA, and the maximum achieved average power in fiber is ~660 μW for V_{SA} = 0 V. For V_{SA} = 1 V, the threshold current is slightly larger than 40 mA, and the maximum fiber-coupled power is ~660 μW. Even though these lie in the typical range of the generic technology [17, 27, 28], but the output power can be further amplified by using on-chip booster amplifier to push the output

(a)

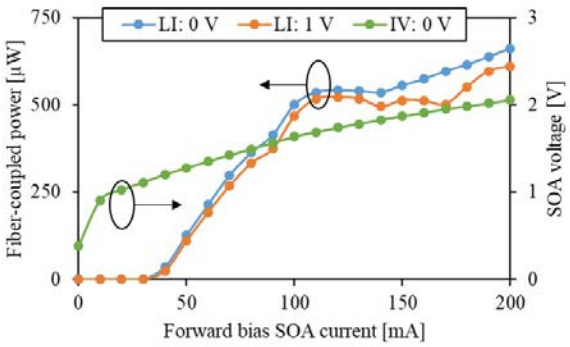

(b)

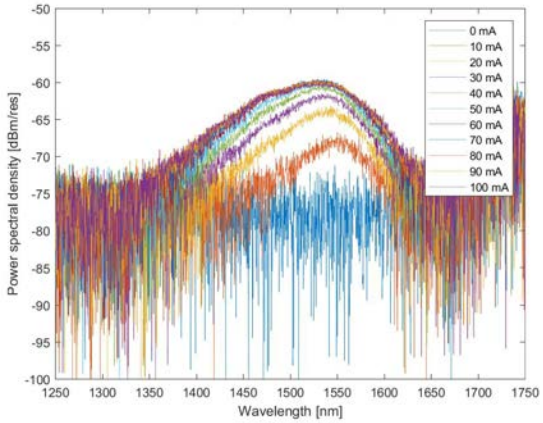

Fig. 3: (a) Light-current-voltage (L-I-V) characteristics of the MLL PIC under test. By sweeping the forward bias gain current I_{SOA} from 0 to 200 mA, the voltage of the parallel gain sections jumps from near zero to 1 V and then smoothly increases up to 2 V for V_{SA} = 0 V (green). The average output power coupled by the lensed fiber also increases, exhibiting a threshold of ~40 mA and a maximum power of ~600 μW for V_{SA} = 1 V (red) and ~660 μW for V_{SA} = 0 V (blue). (b) Amplified spontaneous emission (ASE) spectrum of a 400-μm-SOA with bias current from 0 mA to 100 mA.

power up to a few mW [20].

The output power follows a monotonic trend as I_{SOA} increases, but not in a linear manner. It can be seen that in the first half of the trace the L-I curve exhibits a linear behavior with slope efficiency of ~7.5 mW/A when I_{SOA} = 40 - 100 mA. And the curve becomes less steep with slope efficiency of ~1.5 mW/A when I_{SOA} = 100 - 200 mA. The turning point on the curve might indicate that the laser operates differently in these two regions. The optical spectra in these different operations are experimentally shown in next section. In the whole investigated range that I_{SOA} = 0 - 200 mA, the laser has not reached gain saturation, as no decline is observed on the curve. The upper limit of I_{SOA} is set to 200 mA to avoid damage. The voltage of parallel gain sections lies in the typical range as well. The voltage suddenly rises to ~1 V and afterwards gradually increases to 2 V. Figure 3(b) shows the amplified spontaneous emission (ASE) spectrum of a 400-μm SOA with bias current of 0 - 100 mA. The SOA has a smooth gain profile spanning

(a)

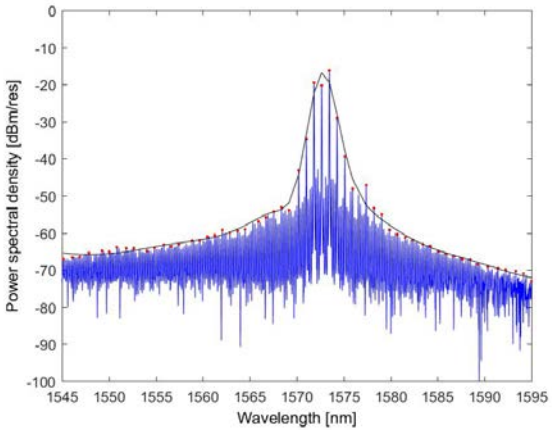

(b)

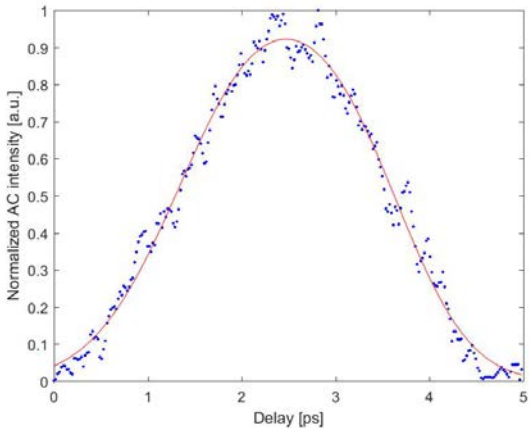

Fig. 4: (a) Optical spectrum with I_{SOA} = 99 mA and V_{SA} = 1 V. (b) Autocorrelation trace I_{SOA} = 99 mA and V_{SA} = 1 V.

over > 100 nm. With bias current of 70 mA and 80 mA, the 1550 nm wavelength region has a broad gain profile > 10 dB.

For evaluating the spectral performance on the wavelength domain, one of the exemplary optical spectra is shown in Fig. 4(a), under I_{SOA} = 99 mA and V_{SA} = 1 V. In the spectrum, an OFC near 1570 nm is presented with seven comb lines and the mode spacing in between is approximately 0.8 nm, equivalent to 100 GHz in frequency. The seven lasing modes constituting the OFC exhibit a suppression ratio of ~30 dB, with respect to the level of the suppressed modes that are associated with the fundamental cavity round trip frequency of 25 GHz. From 1570 to 1575 nm, three modes in every four modes are suppressed, and only one mode in every four modes is excited. This spectral selectivity agrees with the harmonic order of four in the cavity design. A Gaussian-based curve is applied to fit the peaks in the emission spectrum. However, the central mode of the Gaussian shape is not the highest mode. The fitting curve might not perfectly reflect the characteristic of the frequency comb. Also, the number of comb lines is limited, which fails to give an reliable estimated 3-dB bandwidth through the Gaussian fitting curve. In Fig. 4(b),

(a)

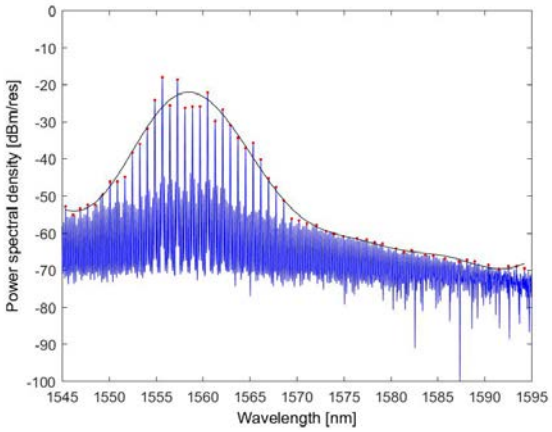

(b)

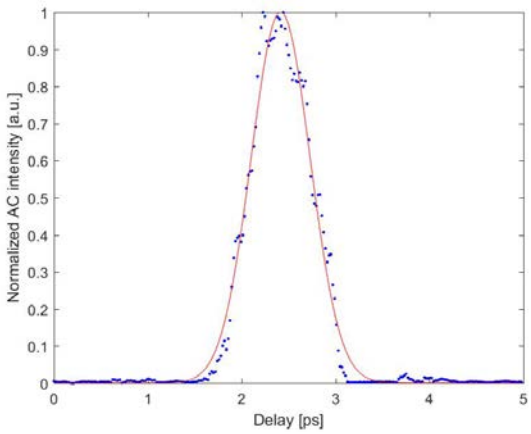

Fig. 5: (a) Optical spectrum with I_{SOA} = 99 mA and V_{SA} = 2.5 V. (b) Autocorrelation trace I_{SOA} = 99 mA and V_{SA} = 2.5 V.

the intensity autocorrelation trace under the same bias condition is shown within a span of 5 ps to evaluate the time-domain performance. The autocorrelation intensities are normalized to scale from 0 to 1. Fitted to a Gaussian function, the FWHM (full width at half maximum) of the autocorrelation profile is about 2.18 ps. The deconvoluted pulse duration is then estimated to be 1.54 ps assuming a Gaussian shape.

Similarly, the optical spectrum and the autocorrelation trace under another bias condition, I_{SOA} = 99 mA and V_{SA} = 2.5 V, are shown in Fig. 5(a) and Fig. 5(b), respectively. The optical spectrum exhibits an optical frequency comb as the optical modes are evenly spaced, with the similar suppression ratio ~30 dB. By contrast, the comb becomes much wider and having more comb lines than that in Fig. 4(a). The emission wavelength also shifts to about 1555 nm, that is ~20 nm away from the emission wavelength of the previous comb. Since there are 25 comb lines within the interval of 1550 - 1570 nm, the fitting curve based on the same algorithm becomes more reliable. With the fitting curve, the estimated 3-dB spectral bandwidth is calculated to be ~0.7 THz. The trace in Fig. 5(b) shows an isolated spike indicative of a pulse. In accordance

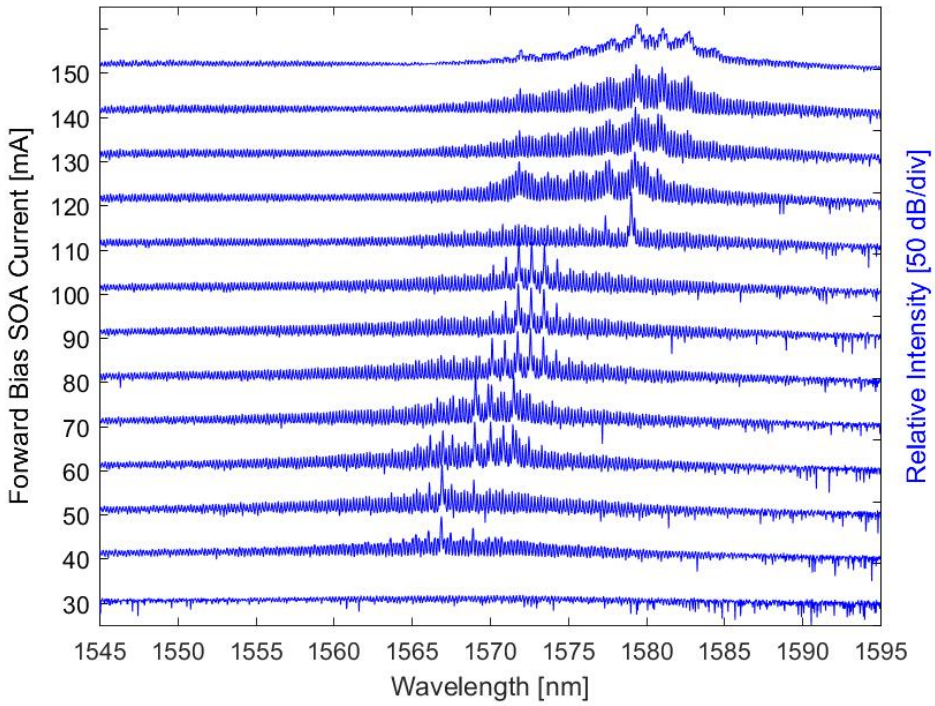

Fig. 6: Evolution of optical spectrum with I_{SOA} = 30 - 150 mA and V_{SA} = 1 V.

with the wider comb in Fig. 5(a), the trace becomes much narrower than that in Fig. 4(b). The zero background indicates a pedestal-free complete mode locking. And the FWHM of trace is 0.71 ps from the fitting Gaussian curve. With a deconvolution factor for Gaussian function 0.707, the retrieved FWHM pulse width is 0.50 ps. It is three times narrower than the pulse width in Fig. 4(b). As shown previously, when properly biased 100-GHz-spacing combs and 500-femtosecond pulses are obtained. Please notice that there is a ~20 nm wavelength jump between the two combs at the selected bias conditions, which is explained in next section.

Figure 6 shows the evolution of spectrum in dependence of I_{SOA}. A series of optical spectra is presented with I_{SOA} varied from 30 to 150 mA and V_{SA} fixed at 1 V. When I_{SOA} = 30 mA, no lasing is observed, as the device is operated below threshold. When I_{SOA} = 40 mA, the device starts lasing around 1567 nm, as the device is just above threshold. As the forward bias current I_{SOA} increases, the multimode emission spectrum shifts to the higher wavelength around 1572 nm. This red shift results from the carrier heating in gain sections. When I_{SOA} is within 80 mA - 100 mA, a few optical modes evenly spaced by 0.8 nm are clearly observed, similar to the optical spectrum shown in Fig. 4(a).

When I_{SOA} increases from 100 mA to 110 mA, the 0.8-nm (100-GHz) comb around 1572 nm collapses and one dominant lasing mode grows around 1578 nm. Furthermore, when I_{SOA} is within 120 mA - 140 mA, broad spectra without harmonic selection are observed. The mode spacing is 25 GHz, corresponding to the fundamental round trip frequency of the 1.66-mm Fabry-Pérot cavity, indicating that the device is in the continuous-wave (CW) Fabry-Pérot operation. Finally, when I_{SOA} = 150 mA, the mode suppression behavior is absent and one can observe the outline of the emission spectrum, indicating the device is in the self-pulsation/Q-switching operation. The mutual coherence information among the 100-GHz optical comb lines can be

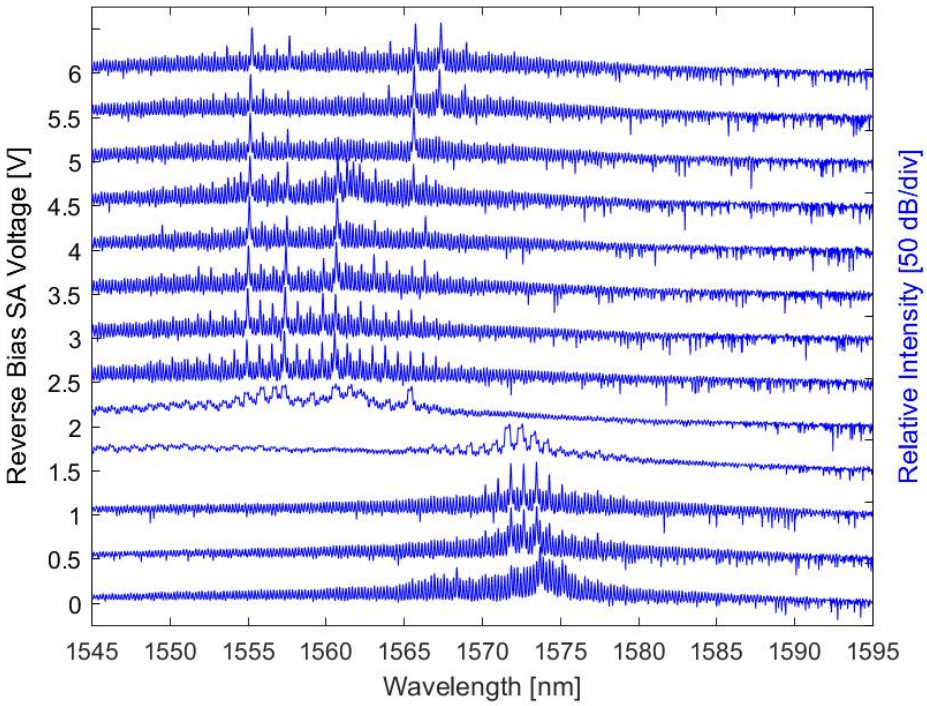

Fig. 7: Evolution of optical spectrum with I_{SOA} = 100 mA and V_{SA} = 0 - 6 V.

extracted from mode beating radio-frequency (RF) spectrum, which can be carried out with a high-speed > 100 GHz photodiode and an ultrawide-bandwidth > 100 GHz electrical spectrum analyzer. The different operation regions at different bias conditions are related to the change in slope efficiency of L-I curve as shown in Fig. 3(a).

Similarly, the evolution of spectra as the reverse bias voltage V_{SA} increases is shown in Fig. 7. In this sequence of optical spectra, the forward bias current I_{SOA} is fixed at 100 mA above threshold, and the reverse bias voltage V_{SA} increases from 0 to 6 V in a step of 0.5 V. When V_{SA} = 0 V, the spectrum in the multimode Fabry-Pérot operation is observed, with 25-GHz mode spacing around the wavelength of 1573 nm. When V_{SA} = 0.5 V and 1 V, optical spectra containing few modes evenly separated by 100 GHz are presented, similar to those shown in Fig. 7 with I_{SOA} is around 100 mA. When V_{SA} increases from 1 V to 1.5 V, the optical spectrum exhibits multiple peaks in a distorted outline. There is a ~20-nm wavelength jump between the spectra at V_{SA} = 1.5 V and V_{SA} = 2 V.

This is because the absorbers are red-drifted. The SA bandgap goes to the red with quantum-confined stark effect-induced shift due to the increased bias voltage. And the spectrum jumps from the regime with minimal losses around the SA band-edge towards the peak of gain in the shorter wavelength, which is around 1555 nm - 1560 nm in this case. Hence, the ~20-nm wavelength jump between V_{SA} = 1 V and V_{SA} = 2.5 V is observed. Apart from the wavelength jump, the transition of regimes occurs from 1 V to 1.5 V and from 2 V to 2.5 V. In the region within 1 - 2 V, the shape is indicative of self-pulsation/Q-switching where the pulse trains are modulated at the relaxation oscillation frequency, usually a few GHz [29].

Above V_{SA} = 2.5 V, wide combs around 1560 nm are achieved, similar to that has been shown in Fig. 5(a). When V_{SA} > 3.5 V, there are few random lasing modes existing around the same

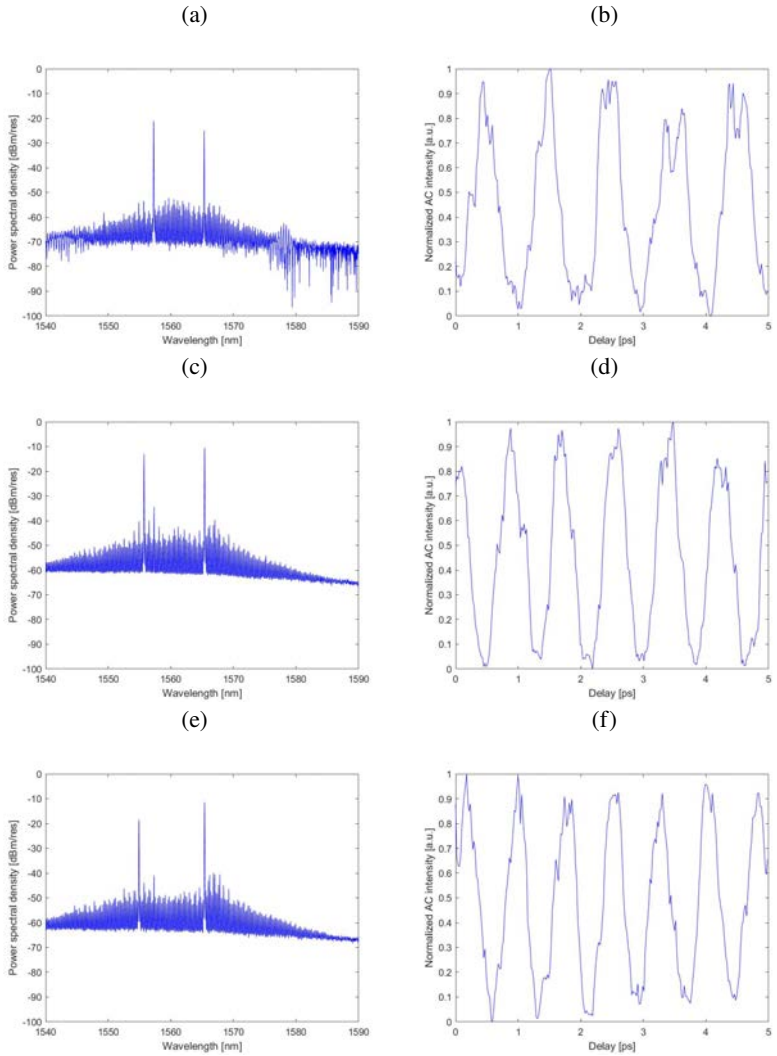

Fig. 8: (a) Optical spectrum, and (b) autocorrelation trace for 1 THz dual-mode emission. (c) Optical spectrum, and (d) autocorrelation trace for 1.2 THz dual-mode emission. (e) Optical spectrum, and (f) autocorrelation trace for 1.3 THz dual-mode emission.

wavelength range. While V_{SA} = 5 V, only two modes occur, with a separation of 1.3 THz. More exemplary dual-mode spectra are experimentally demonstrated along with autocorrelation traces in next section. While $V_{SA} > 5$ V, it seems two groups of modes at 1555 nm and 1565 nm, for which further investigation is required.

The device is capable of generating mode-locked laser. And it can also generate dual-mode laser signals at various rates as shown in Fig. 8 and Fig. 9. When the laser is operated with higher bias levels, it generates higher-order harmonics [8]. In the THz region, the spectral separation between optical lines is too large (> 8 nm) so that the number of optical lines becomes smaller. In such conditions, only two optical modes instead of a huge number of evenly spaced comb lines take place. In Fig. 8(a), two optical lines separated by 1 THz with ~30-dB suppression ratio are shown. And Fig. 8(b) shows the corresponding autocorrelation trace in the period of 1 ps. As there are only two optical lines on the wavelength domain as shown in Fig. 8(a), no matter if they

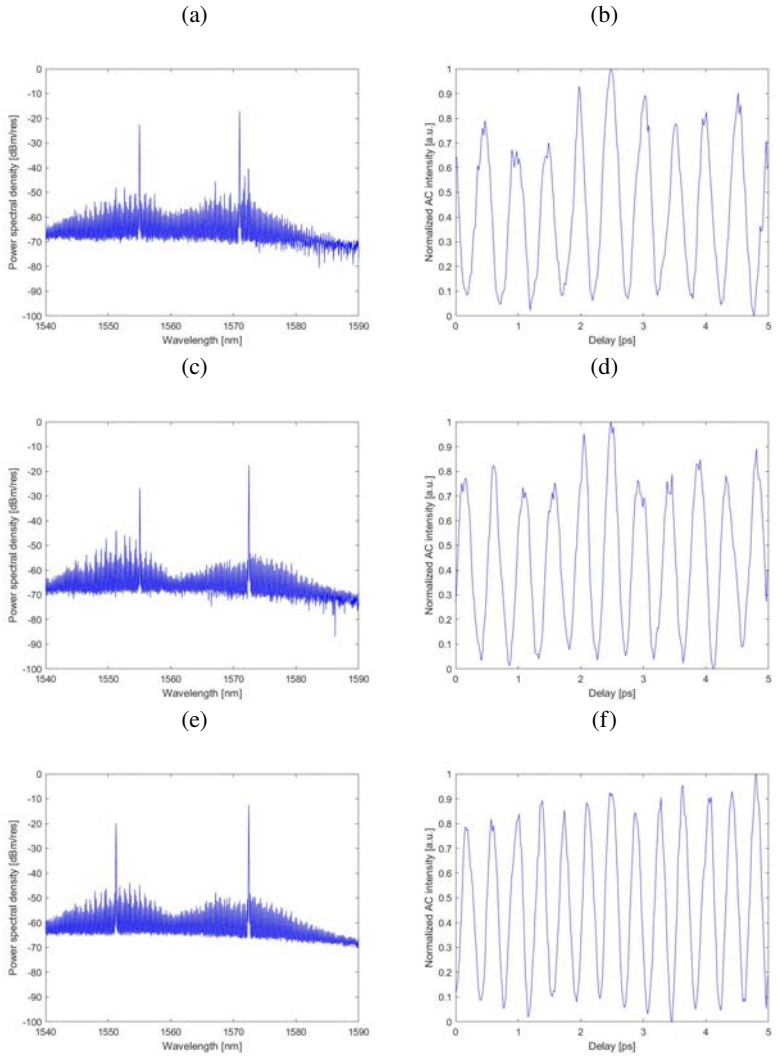

Fig. 9: (a) Optical spectrum, and (b) autocorrelation trace for 2 THz dual-mode emission. (c) Optical spectrum, and (d) autocorrelation trace for 2.2 THz dual-mode emission. (e) Optical spectrum, and (f) autocorrelation trace for 2.7 THz dual-mode emission.

are phase-locked, the autocorrelation trace gives a sinusoidal wave rather than a pulse train. This 1-THz dual-mode laser is achieved with I_{SOA} = 86 mA and V_{SA} = 3.9 V. The bias condition for the 1.2-THz dual-mode signals shown in Fig. 8(c) is I_{SOA} = 99 mA and V_{SA} = 4.4 V. Figure 8(d) shows the sinusoidal trace in 0.83-ps period. Fig. 8(e) is I_{SOA} = 140 mA and V_{SA} = 4.1 V. Figure 8(f) shows the sinusoidal trace in 0.77-ps period. Please notice that for these three THz-rates the SA sections are biased with relatively high voltages (>4 V).

Similarly, Fig. 9(a), Fig. 9(c), and Fig. 9(e) show other three different dual-mode laser signals at even higher THz-rates at 2 THz, 2.2 THz, and 2.7 THz. And their time-domain signals are shown in terms of autcorrelation traces such as Fig. 9(b) in 0.5-ps period), Fig. 9(d) in 0.45-ps period, and Fig. 9(f) in 0.37 ps. All the THz-rates in the exemplary spectra are integer multiple of the fourth harmonic 100-GHz according to the cavity configuration. These higher-order harmonic signals can be used for THz CW generation by photomixing, with the two modes being beat with

a photodiode or photoconductor [24].

4. Conclusion

We have successfully presented an InP mode-locked semiconductor laser for 100-GHz optical frequency comb generation. The pulsewidth amounts into the femtosecond scale - 0.5 ps. Dual-mode generation is also experimentally demonstrated at the various THz rates up to 2.7 THz with higher bias levels. The laser cavity features multiple segments in a symmetric arrangement in which short SOAs separate the overall 1.66-mm-long resonator into four shorter divisions in equal length to achieve fourth harmonic generation. With the generic foundry approach, we have made use of predefined building blocks such as passive waveguides, multimode interference reflectors as on-chip reflectors, and gain/absorber sections (SOA) to realize the design geometry that is fully compatible to the foundry's standard fabrication process in multi-project runs. The on-chip multimode interference reflectors have shown the potential to replace the commonly used but not reliable cleaved facets.

Acknowledgment

The authors thank Dr. Julien Javaloyes for the helpful discussions. This work has been supported by European Union's Horizon 2020 research and innovation programme under the Marie Skłodowska-Curie grant agreement No. 642355 FiWiN5G.